九州大学学術情報リポジトリ
Kyushu University Institutional Repository

Investigation of quantum effect of liquid hydrogen on homogeneous bubble nucleation using a density functional theory and molecular dynamics simulations

Takahashi, Ryuji
Graduate School of Engineering, Kyushu University

Nagashima, Hiroki
Faculty of Engineering, University of the Ryukyus

Tokumasu, Takashi
Institute of Fluid Science, Tohoku University

Watanabe, Satoshi
Department of Mechanical Engineering, Kyushu University

他

https://hdl.handle.net/2324/7170252

出版情報：Fluid Phase Equilibria. 553, pp.113300-, 2022-02-01. Elsevier
バージョン：
権利関係：

KYUSHU UNIVERSITY

Investigation of quantum effect of liquid hydrogen on homogeneous bubble nucleation using a density functional theory and molecular dynamics simulations

Ryuji Takahashi[1], Hiroki Nagashima[2], Takashi Tokumasu[3], Satoshi Watanabe[4], Shin-ichi Tsuda[4]

[1] Graduate School of Engineering, Kyushu University, 744 Motooka, Nishi-ku, Fukuoka 819-0395, Japan

[2] Faculty of Engineering, University of the Ryukyus, 1 Senbaru, Nashihara-cho, Nakagami-gun, Okinawa, 903-0213, Japan

[3] Institute of Fluid Science, Tohoku University, 2-1-1 Katahira Aoba-ku, Sendai, Miyagi, 980-8577, Japan

[4] Department of Mechanical Engineering, Kyushu University, 744 Motooka, Nishi-ku, Fukuoka 819-0395, Japan

Abstract

In this paper, a quantum effect of hydrogen molecules (uncertainties of each atomic nuclear position and momentum) on the bubble nucleation rate was investigated. The homogeneous bubble nucleation analyses were performed using a density functional theory (DFT) reflecting equations of state (EOSs) constructed to reproduce the thermophysical properties of hydrogen obtained from a classical molecular dynamics (MD) method and a quantum MD method. The results showed that the quantum nature of liquid hydrogen decreases the bubble nucleation rate when compared in the same reduced temperature and reduced superheat ratio condition. Further, it was indicated that the results might be caused by the increase of the energy barrier arising from the difference of the density profile and its position at the critical bubble (in other words, the differences of the critical bubble size and the liquid–vapor interface thickness). Furthermore, the DFT analysis was validated through the evaluation of the bubble nucleation rate using the classical MD method and the quantum MD method made as numerical experiments, and qualitatively the same result was obtained between the DFT and the MD simulations.

Keywords : Bubble nucleation, Hydrogen, Quantum effect, Density functional theory, Molecular dynamics method

1. Introduction

Hydrogen has attracted attention as a clean energy alternative to fossil fuels, and it has been used in various devices including fuel cell battery. One of the important issues to achieve a future hydrogen energy society is the efficiency improvement of the storage or transport of hydrogen. To relieve this problem, instead of pressurized gas form, the storage or transport system of hydrogen in liquid form has been recently developed and the establishment of international supply chain has been also progressed [1], because the volume of hydrogen under the atmospheric pressure can be shrunk to 1/800 compared with that in a gaseous state by liquefaction and therefore efficient storage or transport is possible. Since the normal boiling temperature of liquid hydrogen is around 20 K, liquid–vapor phase change by boiling or others (such as cavitation) may easily occur in our daily life conditions, i.e., near room temperature. The liquid–vapor phase change in fluid machines causes the performance decrement, vibration, or noise; therefore, the understanding of the thermal and hydraulic characteristics of fluid devices using liquid hydrogen is necessary for their safe and efficient design and development. Liquid–vapor multiphase flow analyses based on computational fluid dynamics (CFD) techniques are often used to do so. In such analysis, the vapor bubble inception condition should be also somehow given by a model; however, the inception in liquid hydrogen may be caused by homogeneous bubble nucleation different from water as mentioned below. The bubble nucleation rate that will strongly relate to the inception condition in a liquid hydrogen flow has not yet been understood.

In general working fluids such as water, the bubble inception occurs from the pre–existing bubble nuclei which generally contain non–condensable gas or adsorb other impurities. However, since the pre–existing bubble nuclei are considered to be almost absent in liquid hydrogen due to its low temperature [2] and it generally shows a high wettability due to the low surface tension [3, 4], the bubble nucleation may arise from a microscopic void formed by thermal fluctuation of molecules in the bulk liquid (homogeneous bubble nucleation). It was indicated that the consideration of the specific quantum nature of cryogenic hydrogen (uncertainties of the position and momentum of the atomic nucleus) is necessary to simulate such microscopic phenomenon or property [5–7]. Further, the quantum nature is expected to affect the bubble nucleation because it has been confirmed that the quantum nature of liquid hydrogen has a large influence on the saturation line [8]. On the other hand, to our knowledge, experimental investigations of the bubble nucleation in liquid hydrogen have not been done, except an old report by Hord et al. [9]; however, their experimental temperatures are too limited, i.e., the range is 27.8–30.8 K. Considering the fact that a new additional experimental investigation of the homogeneous bubble nucleation in liquid hydrogen is still difficult due to its low temperature, understanding the bubble nucleation rate using a quantum molecular theoretical approach is desirable and necessary.

The theoretical or numerical studies on homogeneous bubble nucleation in classical fluids, i.e., fluids without the mentioned quantum nature such as liquid argon or water have been widely conducted. As a theoretical approach, the

classical nucleation theory (CNT) [10–12] has been typically used to estimate the bubble nucleation rate. However, it is known that the CNT underestimates the bubble nucleation rate because of the capillarity approximation inherently made in the theory [13–17]. Thus, the improvement of the CNT by applications of the Tolman correction [18] and the accurate pre–factor has been discussed by Tanaka et al. [19]. Also, the density functional theory (DFT) [20, 21] which can take account of the continuous density profile near the interface has been proposed to avoid the capillarity approximation. Further, as numerical approaches, the Monte Carlo (MC) simulations or the Molecular dynamics (MD) simulations have been performed to clarify the nucleation process in detail or to provide the test data for the nucleation theories [13–17, 22]. Recently, the homogeneous bubble nucleation analysis using a large–scale MD simulation with 5×10^8 Lennard–Jones (L–J) molecules was also conducted to accurately measure the bubble nucleation rate by Diemand et al. [17].

On the other hand, the theoretical or numerical studies on bubble nucleation for liquid hydrogen as a quantum fluid have hardly been conducted compared with the classical fluids, except the studies on homogeneous bubble nucleation in liquid parahydrogen using the DFT by Navarro et al. [23] and by Pi et al. [24]. Also, as a numerical approach considering the quantum nature, Cao et al. [25] have proposed the path integral centroid MD (CMD) which can reproduce the uncertainty of the position of nucleus at molecular scale. While Nagashima et al. [7, 8] have clarified the quantum effect on the thermophysical properties or the transport properties using the CMD method, to our best knowledge, investigation of the influence of the quantum nature of liquid hydrogen on the bubble nucleation using such microscopic simulations has not been conducted.

This paper aims to clarify the quantum effect of liquid hydrogen on the bubble nucleation rate. In this paper, we performed the analysis of bubble nucleation using the DFT [23] reflecting the equations of state (EOSs) [8] constructed on the basis of the thermophysical properties obtained from the classical MD and the CMD, and the bubble nucleation rates with and without considering the quantum effect were evaluated. We also evaluated the bubble nucleation rate using the classical MD and the CMD simulations as numerical experiments. The validation of the results of DFT analysis was done through the comparison with the result of the MD simulations.

2. Calculation Method

2.1 Evaluation of bubble nucleation rate using a density functional theory

In this section, the expression of the bubble nucleation rate is first shown, then an outline of DFT is presented. Becker and Döring [11] focused on the dynamics of droplet cluster growth in droplet nucleation and formulated the bubble nucleation rate on the basis of the assumption that the cluster size changes only by the adsorption or desorption of monomer, i.e., one–step process. Further, the bubble nucleation rate J_s, which is defined as the number of critical bubbles formed per unit volume and time, is given as Eq. (1) by principally exchanging the liquid and vapor phase in the theory for droplet nucleation,

$$J_\mathrm{s} = \rho_\mathrm{L}\sqrt{\frac{2\gamma}{\pi m B}}\exp\left[-\frac{W_\mathrm{c}}{k_\mathrm{B}T}\right], \tag{1}$$

where ρ_L is number density of bulk liquid at temperature T, m is molecular mass, γ is surface tension at temperature T and k_B is the Boltzmann constant. B is a constant determined from pressure difference between inside and outside of the bubble [12]. The energy barrier W_c is a dominant parameter in nucleation phenomena because the nucleation rate depends exponentially on the energy barrier. In the CNT, the energy barrier is given under the capillarity approximation which regards the continuous density profile in liquid–vapor interface as a step function. However, it is known that the CNT overestimates the energy barrier and underestimates the bubble nucleation rate in some cases because of the approximation [13–17]. Therefore, DFT has been proposed to avoid the capillarity approximation [20, 21].

The DFT for liquid parahydrogen was shown by Navarro et al. [23] following the procedure which was previously employed for liquid helium [26–28]. The approach of the DFT is the same as the density gradient theory [29]. In the general form, the Helmholtz free energy of a bulk system as a density functional is given by Eq. (2),

$$F = \int dr\ \{f_\mathrm{id}(\rho,T) + f_\mathrm{ex}(\rho,T)\}, \tag{2}$$

where f_id and f_ex are the ideal gas term and excess term of the Helmholtz energy density, ρ and T are the number density and temperature, respectively. In this study, each term of the Helmholtz energy density was given assuming hydrogen is consisted of monoatomic molecules for the following reasons. First, since the rotational characteristic temperature of hydrogen is 87.6 K [30] and therefore the rotational motion is not excited in the present low–temperature conditions below the critical temperature of hydrogen, which is around 33 K. Further, the intermolecular potential of hydrogen regarding the excess term can be approximated by the spherical potential because the internuclear distance is very small. In addition, the intermolecular orientations of hydrogen due to diatomic molecules are considered to be hidden

by the apparent spatial spread of molecular position because of the quantum nature. In fact, whereas the thermal de Broglie wave length of hydrogen is about $2-3$ Å in the present temperature conditions and the molecular diameter when assumed as a monoatomic molecule (the L-J parameter regarding the molecular diameter) is about 3 Å, the internuclear distance of hydrogen is only about 0.74 Å [31]. Therefore, both the classical and the quantum system in this study correspond to the monoatomic fluid, i.e., the L-J fluid. The only difference between each system is the presence or absence of the uncertainty of the molecular position. Based on the above, the ideal gas term and excess term of the Helmholtz energy density were given as follows. The ideal gas term of the Helmholtz energy density for a classical system is expressed as follows on the basis of statistical mechanics [32],

$$f_{\mathrm{id}} = \rho k_{\mathrm{B}} T \left(\ln \rho - \ln \left(\frac{2\pi m k_{\mathrm{B}} T}{h^2} \right)^{3/2} - 1 \right), \tag{3}$$

where h is the Plank constant. Note that the form of Eq. (3) was derived by considering only the molecular translational motion. In fact, the ideal gas term of Helmholtz energy density of hydrogen is given as the ideal gas term of the Bose system following the Bose–Einstein statistics [33]. However, since the ideal gas term has little influence for the saturation and spinodal line as shown in appendix A, we conducted the DFT analysis focusing on the quantum effect on the excess term which mainly affects the thermophysical properties. The excess term of Helmholtz energy density for the classical and the quantum system was given by the EOSs which were constructed by Nagashima et al. [8] on the basis of the classical MD and the CMD simulations. The EOSs were constructed using the Kataoka's method [34] based on the function form of the excess Helmholtz free energy F_{ex} as,

$$F_{\mathrm{ex}} = \frac{N}{\beta} \sum_{n=1}^{5} \sum_{m=-1}^{5} A_{nm} \left(\frac{\rho}{\rho_0} \right)^n \left(\frac{\beta}{\beta_0} \right)^m, \tag{4}$$

where $\beta = 1/(k_{\mathrm{B}}T)$, $\rho_0 = 1/\sigma^3$, $\beta_0 = 1/\varepsilon$, N is the number of molecules, and ρ is the number density. ε and σ are the L–J potential parameters shown in Sec. 2.2, and those values were set at $\varepsilon_{\mathrm{H_2}} = 36.5$ K and $\sigma_{\mathrm{H_2}} = 2.96$ Å to reproduce the experimental saturation line of parahydrogen [35] as presented below. According to the thermodynamic relation, the thermophysical properties are expressed using the excess Helmholtz free energy F_{ex}. The 35 expansion coefficients A_{nm} in Eq. (4) for the classical and the quantum system were respectively determined to reproduce the classical MD and the CMD simulation results of the excess internal energy and the pressure using the least square method. The concrete values of the coefficients A_{nm} for each system are shown in appendix B. Note that the same L-J parameters are used in the classical MD and the CMD simulations [8] and thus the difference of the thermodynamic property between the classical and the quantum system as shown in Fig. 1 is caused only by the quantum nature reflected in the CMD simulations. Details on the procedure of construction of the EOSs and the MD simulations can be found in Ref. [8]. Figure 1 shows the saturation and spinodal lines obtained from the EOSs, and we can see the saturation and spinodal lines are largely different due to the quantum nature of the hydrogen molecules. Further, the EOS based on the CMD results can reproduce well the experimental saturation line of parahydrogen [35, 36] except around the critical point. These EOSs were used to provide the thermophysical properties for the DFT calculations of the classical and the quantum system. Using the expansion coefficients A_{nm} for each system, the excess Helmholtz free energy density f_{ex} in Eq. (1) was given as $f_{\mathrm{ex}} = F_{\mathrm{ex}}/V$, where V is the volume.

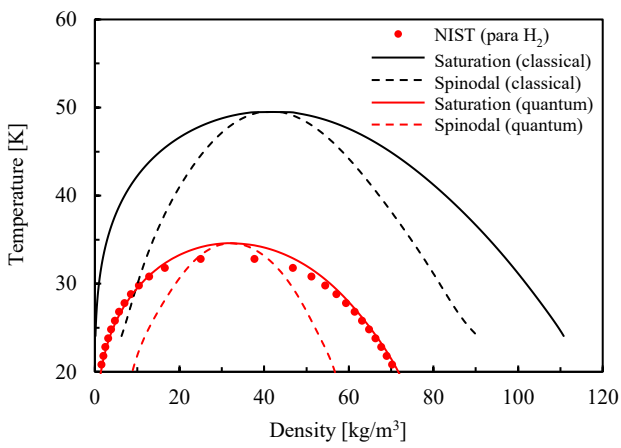

Fig. 1 Comparison of saturation and spinodal lines obtained by each EOS [8]. The minimum temperatures of the classical and the quantum system shown here are respectively 24 K and 20 K, each of which is higher than that of the triple point.

On the other hand, the Helmholtz free energy density for a liquid–vapor system, i.e., a system containing the vapor and the surrounding bulk liquid with the liquid–vapor interface, is given by [23],

$$f = f_{\mathrm{id}}(\rho, T) + f_{\mathrm{ex}}(\rho, T) + \xi(\nabla\rho)^2. \tag{5}$$

The third term on the right side of Eq. (5) is the term related to the surface energy, where the value of ξ was determined to reproduce the experimental surface tension as below. The surface tension can be regarded as excess free energy per unit area and is expressed as [37],

$$\gamma(T) = 2\int_{\rho_{\mathrm{V}}}^{\rho_{\mathrm{L}}} d\rho\, [f(\rho, T) - f(\rho_{\mathrm{V}}, T) - \mu(\rho - \rho_{\mathrm{V}})]^{\frac{1}{2}}\xi^{\frac{1}{2}}, \tag{6}$$

where ρ_{L} and ρ_{V} are the constant densities on the liquid and vapor side of the interface, μ is the chemical potential. We set the value of ξ for the classical and the quantum system to $\xi_{\mathrm{class}} = 15683.2$ KÅ^5 and $\xi_{\mathrm{quant}} = 21574.8$ KÅ^5 so that the experimental data of surface tension [35, 38, 40] at $T/T_{\mathrm{c}} = 0.6$ are reproduced, where T_{c} is critical temperature. In this paper, we referred to the experimental surface tension of oxygen and parahydrogen to determine the values of ξ for the classical and the quantum DFT. Here, for the quantum system, the surface tension of parahydrogen was referred and it is consistent to be that the EOS well corresponds with the experimental saturation line of parahydrogen as shown in Fig. 1. In contrast, there are some fluids which have the same characteristic of thermodynamic properties as the classical system as shown in Figs. 2 and 3; we have chosen oxygen as one of those fluids and its surface tension data were referred for the classical system in this study. Also, to validate the above values of ξ for wide temperature conditions, the comparison of surface tension between the calculated results for the classical and the quantum system using Eq. (6) and the data of oxygen and hydrogen by NIST that can be regarded as experimental data [35, 38, 40] was performed as shown in Fig. 3. Note that the experimental surface tensions in Fig. 3 are non–dimensionalized using the L–J parameters $\varepsilon_{\mathrm{H_2}} = 36.5$ K, and $\sigma_{\mathrm{H_2}} = 2.96$ Å (as mentioned above), $\varepsilon_{\mathrm{O_2}} = 120$ K and $\sigma_{\mathrm{O_2}} = 3.369$ Å, where the values of $\varepsilon_{\mathrm{O_2}}$ and $\sigma_{\mathrm{O_2}}$ were referred to a previous study [41]. As shown in Fig. 3, once the value of ξ is fixed to the value at a given temperature, the surface tension can be well predicted in wide temperature conditions using Eq. (6).

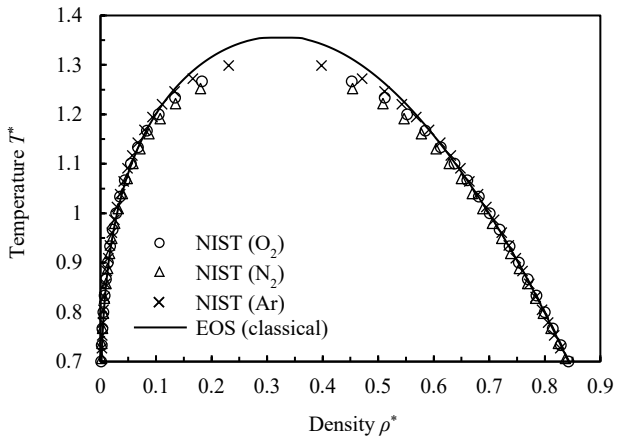

Fig. 2 Comparison of saturation line between the EOS based on the classical MD results and that by NIST data of oxygen, nitrogen and argon [35, 40, 42, 43]. The NIST data are non–dimensionalized by the L–J parameters of $\varepsilon_{\mathrm{O_2}} = 120$ K and $\sigma_{\mathrm{O_2}} = 3.369$ Å, $\varepsilon_{\mathrm{N_2}} = 99.03$ K and $\sigma_{\mathrm{N_2}} = 3.594$ Å, $\varepsilon_{\mathrm{Ar}} = 115.5$ K and $\sigma_{\mathrm{Ar}} = 3.385$ Å [41].

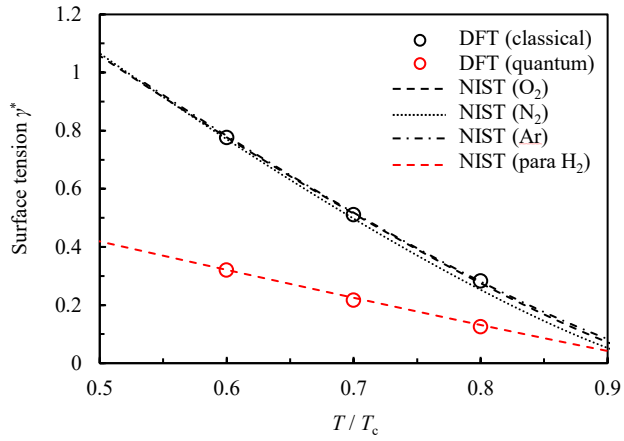

Fig. 3 The calculated surface tension. Open circle: results of DFT using Eq. (6). Dotted line: NIST data of oxygen, nitrogen, argon and parahydrogen [35, 38, 40]. The NIST data are non–dimensionalized using the same L–J parameters with Fig. 2.

Here, since the bubble nucleation phenomenon is generally discussed in grand canonical ensemble, the density profile $\rho(r)$ at a critical bubble nucleus is determined from the variational maximization of the grand potential density $\omega = f - \mu\rho\ (= -p)$, in which p is pressure, leading to the following Euler–Lagrange (E–L) equation.

$$\frac{\delta\omega}{\delta\rho(r)} = \frac{\delta f}{\delta\rho(r)} - \mu = 0, \tag{7}$$

where μ is chemical potential for mother phase, i.e., liquid phase in the present case. Note that the bubble was assumed to be spherical in this study; therefore, the density ρ is only a function of the radial position from the center of the bubble, r. In this study, the E–L equation was numerically solved by shooting method [44]. Using the obtained density profile, the energy barrier is given by Eq. (8) as the integral of local difference between the grand potential density of the liquid–vapor system $\omega_{\mathrm{L-V}}$ and that of the bulk liquid system ω_{L},

$$\begin{aligned} W_{\mathrm{c}} &= \int dr\ 4\pi r^2 [\omega_{\mathrm{L-V}} - \omega_{\mathrm{L}}] \\ &= \int dr\ 4\pi r^2 \left[\left\{f_{\mathrm{id}}(\rho(r),T) + f_{\mathrm{ex}}(\rho(r),T) - \mu\rho(r) + \xi\left(\nabla\rho(r)\right)^2\right\} - \{f_{\mathrm{id}}(\rho_{\mathrm{L}},T) + f_{\mathrm{ex}}(\rho_{\mathrm{L}},T) - \mu\rho_{\mathrm{L}}\}\right], \end{aligned} \tag{8}$$

where $\rho(r)$ is the local number density, ρ_{L} is number density of bulk liquid. Finally, the bubble nucleation rate is obtained from Eq. (1).

In this study, the bubble nucleation analyses for the classical and the quantum system were performed at the same reduced temperature and reduced superheat ratio [45]. The reduced superheat ratio S is given by,

$$S = \frac{\mu_{\mathrm{sat}} - \mu}{\mu_{\mathrm{sat}} - \mu_{\mathrm{spn}}} \approx \frac{p_{\mathrm{sat}} - p}{p_{\mathrm{sat}} - p_{\mathrm{spn}}}, \tag{9}$$

in which the subscript sat or spn corresponds to the values at saturation or spinodal point at a given temperature. Note that the second formula on the right side of Eq. (9) is an approximate but appropriate expression obtained under the assumption that the bulk liquid is incompressible. Shen and Debenedetti [45] reported that the energy barrier is properly scaled by the reduced superheat ratio, and the scaling is valid for the bubble nucleation phenomenon in classical fluids.

2.2 Path integral centroid molecular dynamics method

In this study, we employed the CMD method [25] which can properly simulate the quantum nature at molecular scale and reproduce well the thermophysical and transport properties of liquid hydrogen [6–8]. In the CMD method, the hydrogen molecule is expressed by a ring polymer composed of beads, in which the spatial spread of the beads corresponds to the position uncertainty of the hydrogen molecule [25]. This expression is based on that the quantum partition function corresponds to the classical partition function for a ring polymer composed of beads [46], and we can treat the molecular motion considering the quantum nature by solving the classical equation of motion for the centroid defined as the mass center of beads,

$$m\ddot{\boldsymbol{q}}_i^c = -\frac{\int\cdots\int \prod_{i=1}^{N}\prod_{j=1}^{L} d\boldsymbol{q}_i^{(j)}\delta(\boldsymbol{q}_i^c - \overline{\boldsymbol{q}}_i)\frac{\partial\Phi}{\partial\boldsymbol{q}_i^c}\exp\left(-\beta D\left[\boldsymbol{q}_i^{(j)}\right]\right)}{\int\cdots\int \prod_{i=1}^{N}\prod_{j=1}^{L} d\boldsymbol{q}_i^{(j)}\delta(\boldsymbol{q}_i^c - \overline{\boldsymbol{q}}_i)\exp\left(-\beta D\left[\boldsymbol{q}_i^{(j)}\right]\right)} = \boldsymbol{F}_i^c, \tag{10}$$

where $\boldsymbol{q}_i^c$ and $\boldsymbol{q}_i^{(j)}$ are position of centroid and beads, $\overline{\boldsymbol{q}}_i$ is the average position of Feynmann's path over imaginary time, Φ is the potential acting on the centroid. N is the number of molecules, L is the number of beads per molecule, D is the action integral in imaginary time [25] and $\beta = 1/(k_{\mathrm{B}}T)$. The force on the centroid $\boldsymbol{F}_i^c$ is the average force of beads $\boldsymbol{f}_i^{(j)}$, and is also expressed as follows,

$$\boldsymbol{F}_i^c = \frac{1}{L}\sum_{j=1}^{L}\boldsymbol{f}_i^{(j)} = -\frac{1}{L}\sum_{j=1}^{L}\frac{\partial\phi\left(\boldsymbol{q}_i^{(j)}\right)}{\partial\boldsymbol{q}_i^{(j)}}, \tag{11}$$

where ϕ is the interaction between each pair of the beads and the following L–J potential was employed for the interaction,

$$\phi(d) = 4\varepsilon\left\{\left(\frac{\sigma}{d}\right)^{12} - \left(\frac{\sigma}{d}\right)^{6}\right\}, \tag{12}$$

where ε and σ are the potential parameters corresponding to the well–depth and molecular diameter, respectively, and d is the distance between the pair beads. The potential parameters were set at $\varepsilon_{\mathrm{H_2}} = 36.5$ K and $\sigma_{\mathrm{H_2}} = 2.96$ Å to reproduce the experimental data of saturation line of parahydrogen as shown in the previous section. Other parameters for the CMD simulations were set at the same value with the previous study [8]. In this study, the MD simulations and DFT analyses shown in Sec. 2.1 were performed using in–house FORTRAN codes. Note that, in the next section, all

results are expressed in the non–dimensional unit defined by the molecular mass m and the two L–J potential parameters, ε and σ.

3. Results and discussion

3.1 Analysis of bubble nucleation rate using the DFT

Using the above constructed EOSs, the DFT calculations for the classical and the quantum system were performed in the conditions of the reduced temperatures $T/T_c = 0.6 - 0.8$ and the reduced superheat ratios $S = 0.6 - 0.9$. Figures 4 and 5 show the density profiles around the liquid–vapor interface calculated from Eq. (5) and the interface thicknesses, respectively, at each critical bubble size. The thickness was calculated from the density profile according to the 10–90 thickness [47] defined as the distance in which the density varies from $0.1(\rho_L^* - \rho_V^*)$ to $0.9(\rho_L^* - \rho_V^*)$. As shown in Figs. 4 and 5, we confirmed that the density profile of the quantum system gently varies compared with that of the classical system and the quantum nature consequently increases the interface thickness in the same reduced temperature and reduced superheat ratio condition. In a previous study, Nagashima et al. [8] reported that the quantum nature shallows the well–depth of the intermolecular potential ε and increases the apparent molecular diameter σ. Therefore, the cause of the increase of the interface thickness is considered to be the increase of intermolecular distance by that the quantum nature decreases the intermolecular attractive interaction and increases the molecular diameter. Further, it was suggested that the liquid and vapor density decrease because of the increase of the apparent molecular diameter due to the quantum nature. Figure 6 shows the critical bubble radius of the classical and the quantum system which are calculated as the position of Gibbs (equimolar) dividing surface [47] from each density profile. We also confirmed that the critical bubble radius of the quantum system increases compared to that of the classical system. This is caused by not only the increase of the interface thickness but also the change of the position where density is $0.1(\rho_L^* - \rho_V^*)$ regarded as a boundary position of the vapor region. For example, at $T/T_c = 0.6$ and $S = 0.6$ (the black lines shown in Fig. 4), the boundary positions of the classical and the quantum system are 2.15 [–] and 3.39 [–], and the interface thickness of the classical and the quantum system are 2.31 [–] and 3.65 [–], respectively.

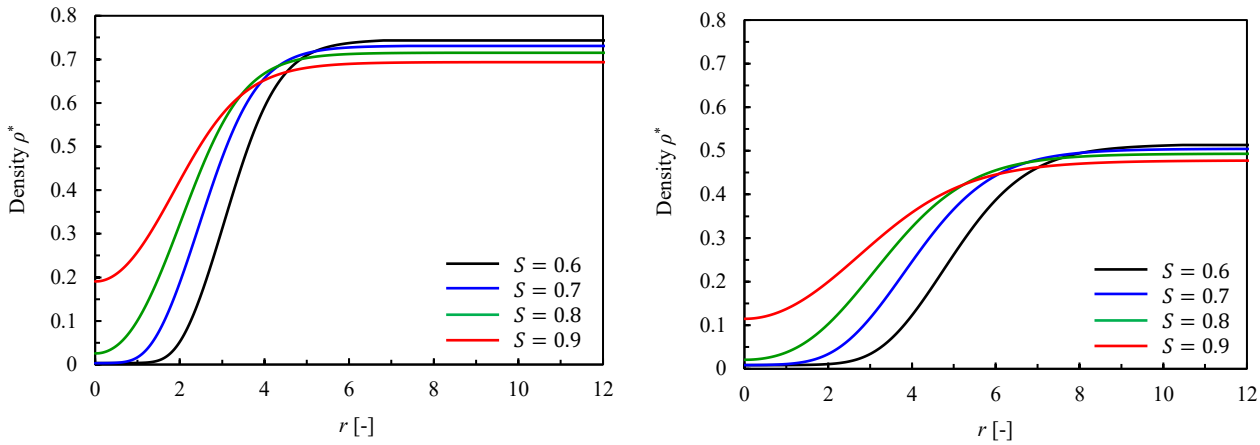

Fig. 4 Density profiles around the liquid–vapor interface calculated for the classical system (left) and the quantum system (right) at $T/T_c = 0.6$.

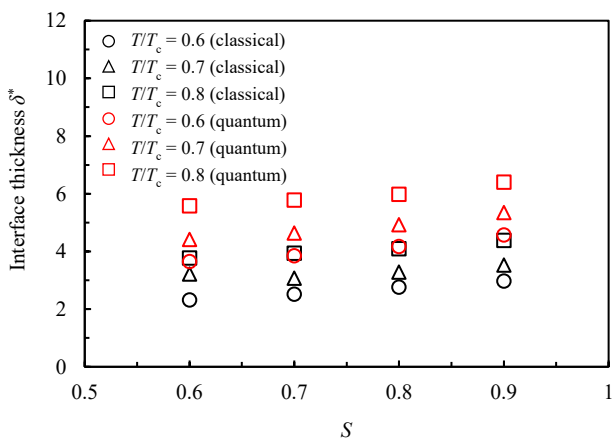

Fig. 5 Comparison of the interface thickness between the classical and the quantum system.

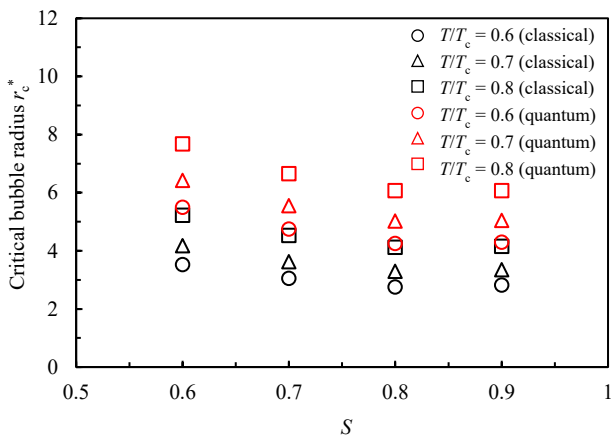

Fig. 6 Comparison of the critical bubble size between the classical and the quantum system.

According to the density profiles obtained from E–L equation, each energy barrier W_c^* was calculated as the difference of the grand potential between the critical system and the bulk liquid system from Eq. (8). Figure 7 shows the energy barrier W_c^* and that reduced by T^*. As shown in the figure, the energy barrier W_c^* was weakly dependent on temperature as with the previous study [45], and the quantitative difference of the energy barrier W_c between the classical and the quantum system was small. Whereas, the energy barrier reduced by the order of the thermal kinetic energy, W_c^*/T^* $(= W_c/k_B T)$, of the quantum system was explicitly larger than that of the classical system when compared in the same reduced temperature and reduced superheat ratio condition. Thus, the variation of the reduced energy barrier W_c^*/T^* between the classical and the quantum system arose from the difference of the temperature T^* between each system. Here, since the grand potential density is given as $\omega = f - \mu\rho$, and the Helmholtz energy density f of liquid–vapor system is given as total of the surface energy and the bulk energy (volume energy) shown in Eq. (5), the energy barrier W_c calculated as the difference of the grand potential can be divided into the terms pertaining to the surface energy or the volume energy. Based on the above, as the components of the reduced energy barrier W_c^*/T^*, the reduced surface energy W_{surf}^*/T^* and that of the volume energy W_{vol}^*/T^* are shown in Fig. 8. Note that the surface energy W_{surf} and the volume energy W_{vol} correspond to the integral of only $\xi(\nabla\rho)^2$ and that of the other terms in Eq. (8), respectively. As shown in the figure, we confirmed that the quantum nature increases the surface energy and decreases the volume energy. Additionally, the distribution of the surface energy and that of the volume energy are shown in Fig. 9 as local energy W_{local}^*. The local surface energy $W_{\mathrm{local,surface}}$ and the local volume energy $W_{\mathrm{local,volume}}$ are given by Eq. (13) and (14),

$$W_{\mathrm{local,surface}}(r) = 4\pi r^2[\xi\{\nabla\rho(r)\}^2], \tag{13}$$

$$W_{\mathrm{local,volume}}(r) = 4\pi r^2[\{f_{\mathrm{id}}(\rho(r),T) + f_{\mathrm{ex}}(\rho(r),T) - \mu\rho(r)\} - \{f_{\mathrm{id}}(\rho_{\mathrm{L}},T) + f_{\mathrm{ex}}(\rho_{\mathrm{L}},T) - \mu\rho_{\mathrm{L}}\}]. \tag{14}$$

From Fig. 9, we confirmed that the maximum and minimum values of the surface or volume energy are almost the same between the classical and the quantum system. Whereas, those energy distributions of the quantum system spread and locate away from the center of a critical bubble than that of the classical system. This is due to the increase of the interface thickness and the vapor region, i.e., the resulting critical bubble radius, mentioned above. Therefore, on the basis of the reduced surface energy W_{surf}^*/T^* and that of the volume energy W_{vol}^*/T^* given as the integral of the local values in the figure, we confirmed that the surface energy increases because of the increase of the interface thickness and the volume energy decreases because of the increase of critical bubble radius (the increase of vapor phase region in other words). As a result, the reduced energy barrier W_c^*/T^* of the quantum system is higher than that of the classical system because the influence of the increase of the surface energy W_{surf}^*/T^* is larger than that of the decrease of the volume energy W_{vol}^*/T^*. Figure 10 shows the distributions of the surface energy and the volume energy, in which the horizontal axis is reduced by the critical bubble radius r_c^* shown in Fig. 6. From the figure, we confirmed that those energy distributions of the classical and the quantum system corresponded well. This result indicated that the quantum effect on the reduced energy barrier W_c^*/T^* might be scaled by the two macroscopic parameters, the order of the thermal kinetic energy T^* $(= k_B T/\varepsilon)$ and the critical bubble radius r_c^*, regardless of temperature conditions. Figure 11 shows the bubble nucleation rate obtained by substituting the energy barrier for Eq. (1). The bubble nucleation rate of the quantum system is small compared with that of the classical system in the same reduced temperature and reduced superheat ratio condition. These results indicated that the quantum nature of liquid hydrogen varies the density profile of the critical bubble by the changes in the intermolecular interaction of the hydrogen molecules [8] as mentioned above, and results in the increase of the energy barrier and the decrease of the bubble nucleation rate.

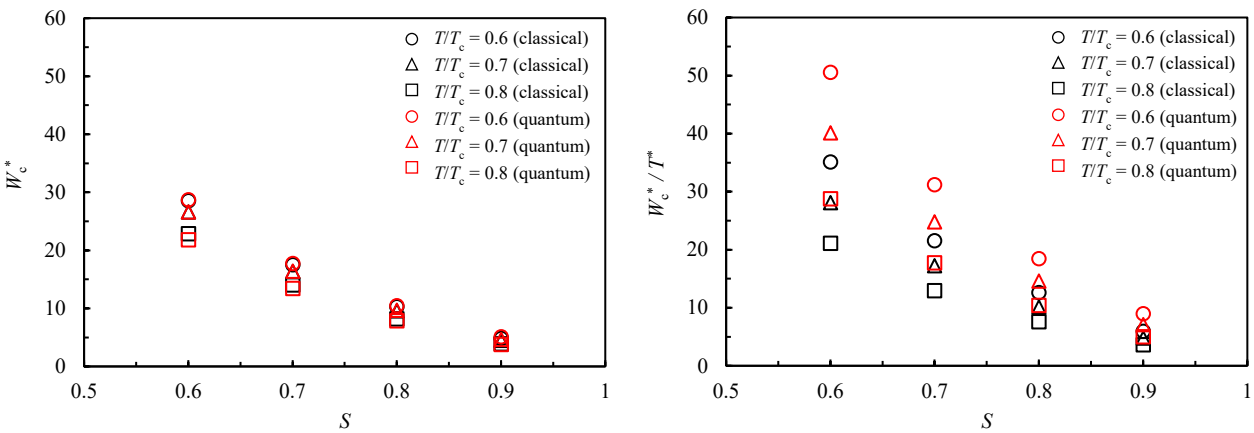

Fig. 7 Comparison of the energy barrier (left) and the reduced energy barrier (right) between the classical and the quantum system.

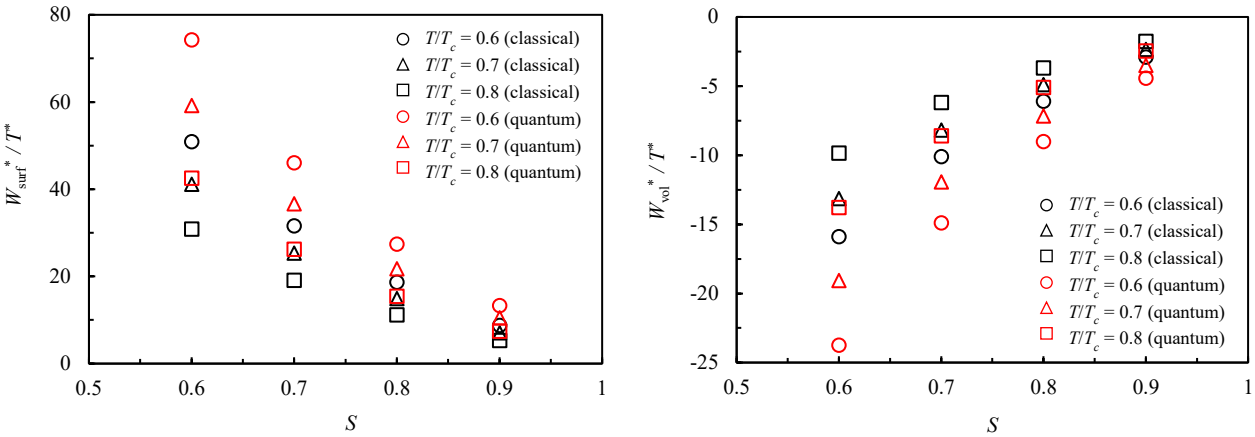

Fig. 8 Comparison of the reduced surface energy (left) and the reduced volume energy (right) between the classical and the quantum system.

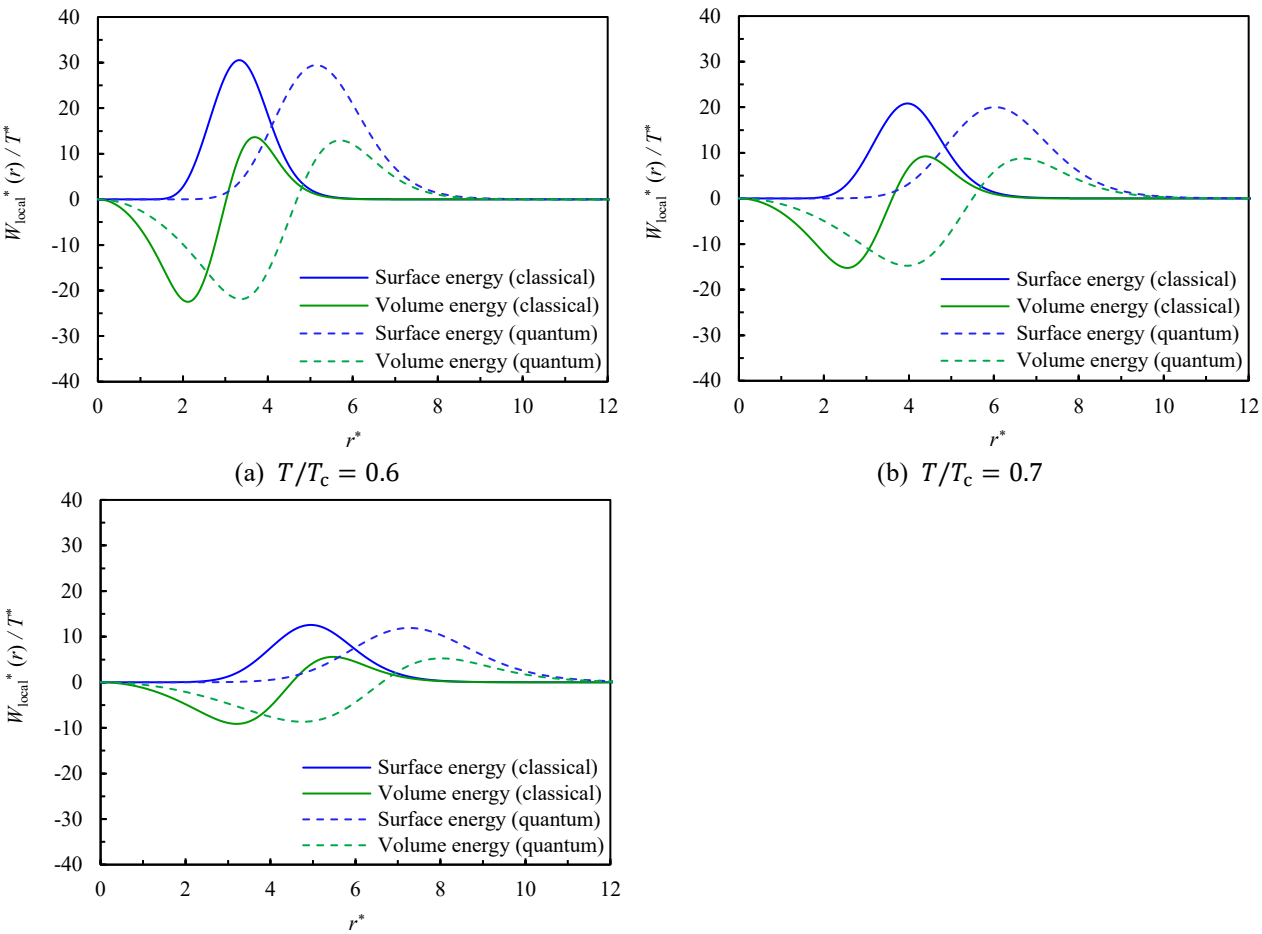

(a) $T/T_c = 0.6$

(b) $T/T_c = 0.7$

(c) $T/T_c = 0.8$

Fig. 9 The distributions of the reduced surface energy and the reduced volume energy for the classical system and the quantum system at $S = 0.6$: (a) $T/T_c = 0.6$, (b) $T/T_c = 0.7$, (c) $T/T_c = 0.8$.

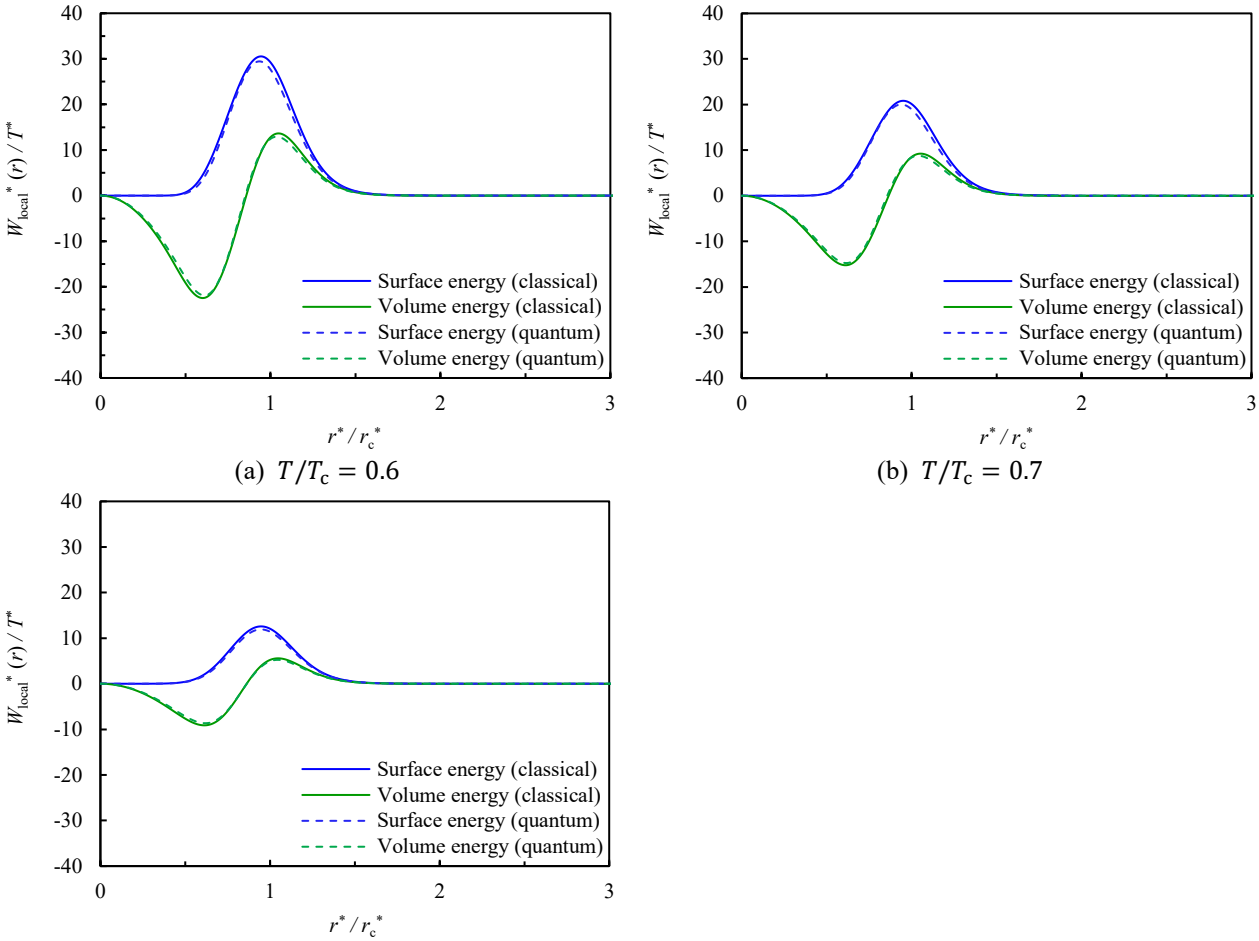

Fig. 10 The distributions of the reduced surface energy and the reduced volume energy for the classical system and the quantum system at $S = 0.6$: (a) $T/T_c = 0.6$, (b) $T/T_c = 0.7$, (c) $T/T_c = 0.8$. The horizontal axis is the distance from center of bubble reduced by critical bubble radius r_c^*.

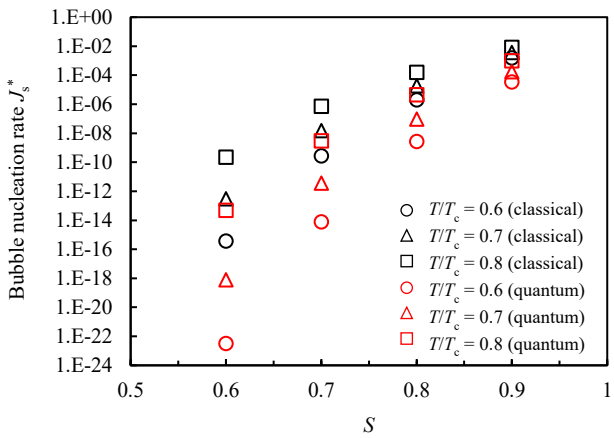

Fig. 11 Comparison of bubble nucleation rate between the classical and the quantum system.

3.2 Evaluation of bubble nucleation rate using MD simulation

For the validation of the results obtained from DFT analysis, we also performed the MD simulations of homogeneous bubble nucleation in the liquid with a high reduced superheat ratio ($S = 0.8$), in which bubble nucleation occurs in a relatively short time that can be directly monitored by MD simulations as numerical experiments. In the present CMD calculations, we set 8 beads for each molecule from viewpoint of calculation cost. Previously, that at least about 30 beads are required for each molecule to quantitatively reproduce the quantum effect of liquid hydrogen was confirmed [43]. However, since the constructed EOS based on CMD with 8 beads relatively reproduce the experimental saturation line compared with the EOS of classical system as shown in appendix C, we judged that the quantum effect on bubble nucleation rate can be qualitatively evaluated even by the CMD with 8 beads. The number of molecules was 10976, and we set the periodic boundary condition for all directions on a cubic simulation domain. The reference system propagator algorithm method [49] was employed as the numerical integration method, and the time steps to solve the equation of motion of the centroids and beads were set at 0.2 fs and 0.02 fs, respectively. In this simulation, first classical MD simulation was performed during first 1 ps, then switched to the CMD simulation. After the CMD simulation in the canonical ensemble using Nosé–Hoover chain thermostats [50] during 4 ps to prepare the equilibrium state at around saturation liquid state, the simulation domain was isotropically expanded in one step to enhance homogeneous bubble nucleation in decompressed metastable liquid state. During 4 ps after the expansion, the above temperature control was continued because the temperature of the system decreases by the adiabatic expansion. After that, the CMD simulation in the microcanonical ensemble was performed.

First, the void region where there is no molecule was judged using Maruyama and Kimura's method [51] and the volume of void region was evaluated. The typical time history of a void volume is shown in Fig. 12. Note that at time $t = 0$ ps of transverse in Fig. 12 corresponds to the start time of MD simulation in the microcanonical ensemble. From the figure, the void volume is first maintained at approximate constant a certain time. Then, the void volume rapidly grows, and a bubble regarded as the aggregate of voids is generated. The time during the initial maintained void volume is called waiting time, and the bubble nucleation rate was evaluated from the waiting time. We conducted 100 simulations with different combinations of initial position and velocity of molecules and evaluated 100 waiting time for each classical and quantum system. The bubble nucleation rate can be calculated from the time variation of the number of survival (non–nucleated) samples $n(t)$,

$$J_s = -\frac{1}{tV}\ln\left(\frac{n(t)}{n(0)}\right), \tag{15}$$

where t is time, V is volume of the simulation domain [13, 52]. Substituting the gradient of approximate straight line in Fig. 13 for $\ln\big(n(t)/n(0)\big)/t$ in Eq. (15), each bubble nucleation rate for the classical and the quantum system was obtained as shown in Table 1. Here, we employed the initial steep gradient where the statistical accuracy is ensured [13, 52]. As shown in Table 1, the bubble nucleation rates of the classical system obtained from the MD simulation and the DFT seem to correspond within the relatively small deviation about one order. However, since it was indicated that the bubble nucleation rate is affected by the domain size of the MD simulation in previous studies [17, 53], the domain size of the present MD simulation might not be enough for the detailed discussion on the quantitative difference of the bubble nucleation rate from that by the DFT. For example, the bubble nucleation rate obtained from the MD simulation with 8000 atoms by Wu et al. [53] is about two order larger than that obtained from the MD simulation with 5×10^8 atoms by Diemand et al. [17]. From these results, it is expected that the bubble nucleation rate decreases and the difference from that by the DFT increases considering the larger domain than the present MD simulation. In this study, the qualitative effect of the quantum nature on the bubble nucleation rate was focused assuming that the bubble nucleation rates for both of the classical MD and the CMD simulation similarly decrease due to the size effect of the simulation domain. We confirmed that the quantum nature reduces the bubble nucleation rate in the same reduced temperature and reduced superheat ratio condition, and this result qualitatively corresponds to that of the present DFT analysis. The quantitative difference of the bubble nucleation rate between the classical and the quantum system was small as compared with the result of the DFT analyses, one of the causes would be that the present CMD with 8 beads did not quantitatively reproduce the quantum nature considering that the CMD with 8 beads cannot reproduce exactly the experimental saturation line of parahydrogen compared with the CMD with 64 beads as show in appendix C. Therefore, for more quantitative validation of the present DFT results, the CMD simulations with the larger number of beads and the larger simulation domain is necessary. However, the present MD results as numerical experiments show that the present DFT results, i.e., the decrease of bubble nucleation rate by the quantum effect, will be qualitatively correct.

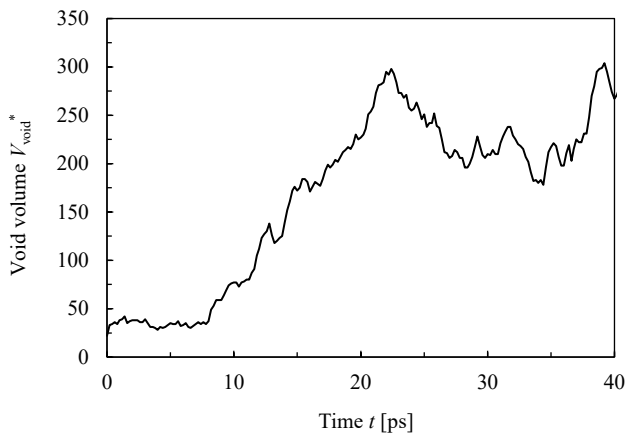

Fig. 12 Example of time history of void volume in the CMD simulation.

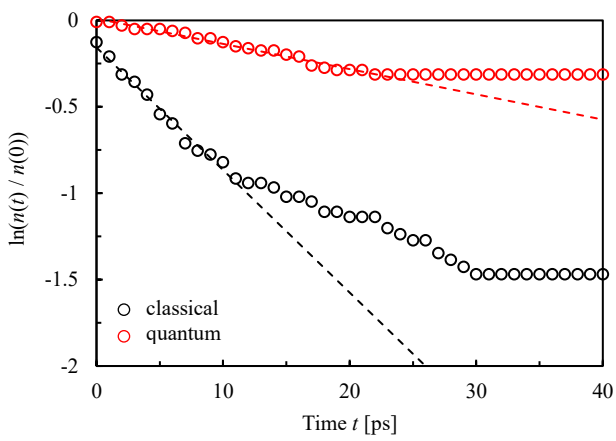

Fig. 13 Survival probability of each system in the MD simulations.

Table 1 Bubble nucleation rates J_s^* obtained from the DFTs and the MD simulations at $T/T_c = 0.7$ and $S = 0.8$

	Classical	Quantum
MD	3.24×10^{-6}	0.509×10^{-6}
DFT	19.0×10^{-6}	0.0968×10^{-6}

4. Conclusions

We have investigated the effect of quantum nature of liquid hydrogen on the homogeneous bubble nucleation rate using the DFT with MD simulations. The DFT results showed that the quantum nature decreases the bubble nucleation rate in the same reduced temperature and reduced superheat ratio condition, and it was indicated that the result was caused by the difference of the density profile at the critical bubble size. We additionally confirmed that the DFT results are qualitatively consistent to the bubble nucleation rates using the classical MD and the CMD simulations as numerical experiments, which can support the validity of the DFT result at least qualitatively. In other words, these results indicated that the simple scaling by the reduced temperature and the reduced superheat ratio might not be valid for a bubble nucleation in quantum liquids. On the other hand, it was indicated that the quantum effect on the energy barrier height might be scaled by the two macroscopic parameters, the temperature and the critical bubble radius. Clarification of the relation between those macroscopic parameters and the microscopic effective potential parameters, the latter of which changes due to the quantum nature shown by Nagashima et al. [8], and finding an appropriate scaling between the classical and the quantum fluid are the next interesting problems.

Acknowledgments

This study has been supported by the Grant–in–Aid for JSPS Fellows 20J12642, Iwatani Naoji Foundation, and the Collaborative Research Project of the Institute of Fluid Science, Tohoku University. Also, the authors especially thank to Mr. Daiki Yasui, who was a former graduate student in Kyushu University, for his introducing the basis of the DFT analysis.

Appendix

A. The quantum effect on the ideal gas term of the Helmholtz free energy

Here, the influence of the difference in the ideal gas term on the saturation and the spinodal lines is presented. The classical ideal gas term of the Helmholtz free energy was employed in the both DFT analyses for the classical and the quantum system in this paper. The accurate ideal gas term of the Helmholtz free energy density for parahydrogen is given by Eq. (A.1) according to the Bose–Einstein statistics,

$$f_{\mathrm{id,Bose}} = \rho k_{\mathrm{B}} T \ln z - \frac{k_{\mathrm{B}} T}{\lambda^3} g_{5/2}(z), \tag{A.1}$$

where λ is the thermal de Broglie wave length given as $\lambda \equiv \sqrt{h^2/2\pi m k_{\mathrm{B}} T}$. g is the function defined as $g_p(z) \equiv \sum_{l=1}^{\infty} z^l/l^p$ and z is the fugacity defined as,

$$z = \begin{cases} 1 & \text{if } \rho\lambda^3 \geq g_{3/2}(1) \\ z_0 & \text{if } \rho\lambda^3 < g_{3/2}(1) \end{cases}, \tag{A.2}$$

where z_0 is the root of the equation, $\rho\lambda^3 = g_{3/2}(z)$ [33]. The saturation and spinodal lines were calculated from the EOSs constructed by the Kataoka's method [34] coupled with the ideal gas term of the Helmholtz energy density for the classical system (Eq. (3)) and the Bose system (Eq. (A.1)) as below. From the thermodynamic relation, pressure p can be expressed as follows using the Helmholtz energy density $f = f_{\mathrm{id}} + f_{\mathrm{ex}}$,

$$p = \rho^2 \left(\frac{\partial}{\partial \rho} \left(\frac{f_{\mathrm{id}}}{\rho} \right) \right)_T + \rho k_{\mathrm{B}} T \sum_{n=1}^{5} \sum_{m=-1}^{5} A_{nm} n \left(\frac{\rho}{\rho_0} \right)^n \left(\frac{\beta}{\beta_0} \right)^m. \tag{A.3}$$

Note that the second term on the right hand side of Eq. (A.3) was derived from the expression of the excess Helmholtz energy given by Eq. (4), and the same expansion coefficients A_{nm} for the excess term was given to confirm only the influence by the ideal gas term. Using the obtained pressure–density curves at each temperature from Eq. (A.3), the saturation point was calculated so that the pressure and the chemical potential of the liquid phase and those of the vapor phase are respectively equal [30]. Further the spinodal point was calculated as the density where $(\partial p/\partial \rho)_T = 0$ is satisfied. Figure A.1 shows the comparison of the saturation and the spinodal lines obtained from the EOSs using ideal gas term of classical or ideal gas term of the Bose system. As shown in the figure, each of the saturation and spinodal lines is shifted up by considering the quantum nature for the ideal gas term. However, we can see that the quantitative difference by the ideal gas term is small.

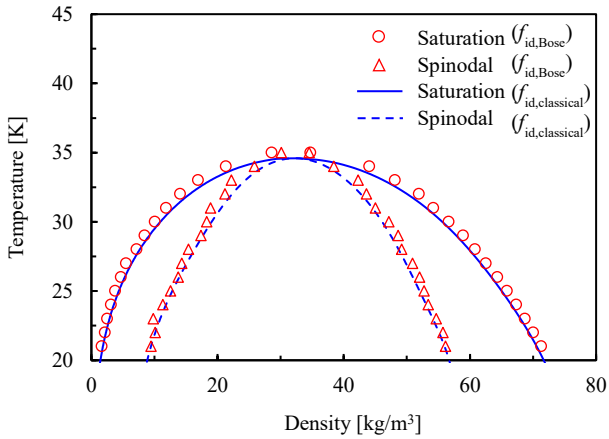

Fig. A.1 Saturation and spinodal lines obtained from the EOSs reflecting the ideal Helmholtz energy of the classical and the Bose system.

B. The expansion coefficients of the EOSs

The coefficients A_{nm} of the EOSs for the classical and the quantum system are presented. From the thermodynamic relation, the pressure and the potential energy are expressed using the excess Helmholtz energy as follows.

$$U_{\mathrm{ex}} = \left\{ \frac{\partial(\beta F_{\mathrm{ex}})}{\partial \beta} \right\}_\rho, \tag{B.1}$$

$$p = \left(\frac{\rho}{\beta} \right) \left[1 + \rho \left\{ \frac{\partial}{\partial \rho} \left(\frac{\beta F_{\mathrm{ex}}}{N} \right) \right\}_\beta \right]. \tag{B.2}$$

The values of coefficients A_{nm} in Eq. (4) were determined so that the pressure p and the potential energy U_{ex} calculated from the classical MD or the CMD are well reproduced using least square method. Here, the temperature ranges of the referenced MD data are about $T = 24 - 70$ K and $T = 14 - 50$ K for the classical and the quantum system [8], respectively. The resulting 35 coefficients for each of the classical and the quantum system are shown in Table B.1.

Table B.1 Coefficients A_{nm} in the EOSs.

Classical system			Quantum system		
n	m	A_{nm}	n	m	A_{nm}
1	-1	-1.029251E+01	1	-1	1.670957E+02
1	0	8.092454E+01	1	0	-8.472937E+02
1	1	-2.548110E+02	1	1	1.749834E+03
1	2	4.060925E+02	1	2	-1.886927E+03
1	3	-3.637892E+02	1	3	1.111972E+03
1	4	1.664662E+02	1	4	-3.408568E+02
1	5	-3.052595E+01	1	5	4.248982E+01
2	-1	3.535638E+01	2	-1	-1.838741E+03
2	0	-2.383210E+02	2	0	9.394093E+03
2	1	6.422277E+02	2	1	-1.949799E+04
2	2	-8.549804E+02	2	2	2.103187E+04
2	3	5.873190E+02	2	3	-1.241816E+04
2	4	-1.803162E+02	2	4	3.805882E+03
2	5	1.509516E+01	2	5	-4.731820E+02
3	-1	-4.759112E+01	3	-1	6.733856E+03
3	0	2.309243E+02	3	0	-3.447921E+04
3	1	-2.771112E+02	3	1	7.168962E+04
3	2	-3.265888E+02	3	2	-7.740421E+04
3	3	9.983890E+02	3	3	4.572170E+04
3	4	-8.019189E+02	3	4	-1.400463E+04
3	5	2.163155E+02	3	5	1.738286E+03
4	-1	3.198374E+01	4	-1	-1.023013E+04
4	0	-6.349142E+01	4	0	5.245561E+04
4	1	-3.976525E+02	4	1	-1.091592E+05
4	2	1.680099E+03	4	2	1.179101E+05
4	3	-2.434304E+03	4	3	-6.965220E+04
4	4	1.561727E+03	4	4	2.132367E+04
4	5	-3.751708E+02	4	5	-2.643783E+03
5	-1	-9.600149E+00	5	-1	5.564253E+03
5	0	-7.320356E+00	5	0	-2.856436E+04
5	1	2.893069E+02	5	1	5.948831E+04
5	2	-9.210605E+02	5	2	-6.427604E+04
5	3	1.229739E+03	5	3	3.797241E+04
5	4	-7.553655E+02	5	4	-1.162143E+04
5	5	1.762989E+02	5	5	1.439858E+03

C. The effect of number of beads in the CMD simulation

Here, we show the effect of number of beads in the CMD on the thermophysical properties. In the CMD method, the basic equations have been formulated using the relation that the classical partition function for a ring polymer composed of beads corresponds to the quantum partition function only in the limit of infinite number of beads. However, since infinite number of beads cannot be treated in actual CMD simulation, the CMD with enough number of beads is regarded as good approximation. The dependency of the number of beads on the thermophysical properties is reported by Nagashima et al. [48]. For reference, we show the comparison of the saturation lines obtained from the EOS which was constructed on the basis of the CMD simulations with 8 or 64 beads in Fig C.1. Here, the CMD simulations with 8 beads were performed using the same calculation conditions with Nagashima et al. [8] except the number of beads. The EOS reflecting the CMD results was also constructed by the Kataoka's method. As shown in Fig. B.1, we can see that the CMD with 8 beads can fairly reproduce the experimental saturation line compared with the classical MD although the quantitative deviation from the NIST data is remained.

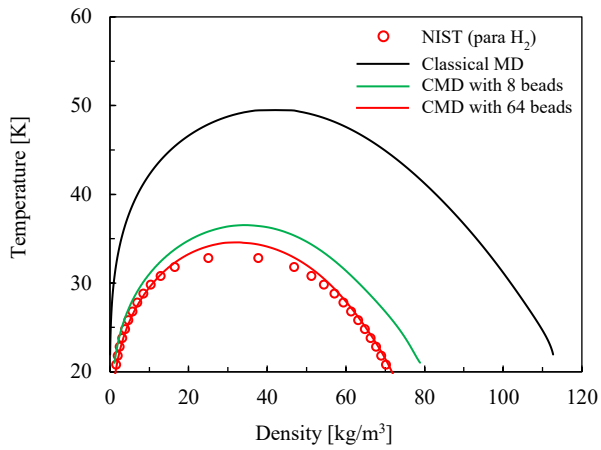

Fig. C.1 Comparison of saturation lines given by the EOSs based on the classical MD or the CMD with 8 or 64 beads [8].

Nomenclature

A_{nm}	Coefficients for equation of state $[-]$
B	Constant on mechanical equilibrium of bubble $[-]$
d	Intermolecular distance [m]
D	Action integral [J]
f	Helmholtz energy density $[\mathrm{J/m^3}]$
F	Helmholtz free energy [J]
h	Plank constant $[\mathrm{J \cdot s}]$
J_s	Bubble nucleation rate $[1/(\mathrm{m^3 \cdot s})]$
k_B	Boltzmann constant [J/K]
L	Number of beads $[-]$
m	Molecular mass [kg]
n	Number of non–nucleated samples $[-]$
N	Number of molecules $[-]$
p	Pressure $[\mathrm{N/m^2}]$
r	Radial coordinate [m]
r_c	Critical bubble radius [m]
S	Reduced superheat ratio $[-]$
t	Time [ps]
T	Temperature [K]
T_c	Critical temperature [K]
U	Potential energy [J]
V	Volume $[\mathrm{m^3}]$
W_c	Energy barrier [J]
z	Fugacity $[-]$
$\boldsymbol{q}_i^c$	Position of centroid
$\boldsymbol{q}_i^{(j)}$	Position of beads
$\bar{\boldsymbol{q}}_i$	Average position of Feynmann's path
$\boldsymbol{F}_i^c$	Force on the centroid
$\boldsymbol{f}_i^{(j)}$	Average force of beads

Greek Letters

β	Inverse temperature $[1/\mathrm{J}]$
γ	Surface tension $[\mathrm{N/m}]$
δ	Interface thickness [m]
ε	Lennard-Jones potential parameter [J]
λ	Thermal de Broglie wave length [m]
μ	Chemical potential [J]
ξ	Constant for surface energy $[\mathrm{K \cdot Å^5}]$

ρ	Number density $[1/\mathrm{m}^3]$
σ	Lennard-Jones potential parameter [m]
ϕ	Intermolecular pair potential [J]
Φ	Potential acting on the centroid
ω	Grand potential density $[\mathrm{J}/\mathrm{m}^3]$

Subscripts

Ar	Argon
ex	excess term
id	ideal gas term
L	Liquid
V	Vapor
$\mathrm{L-V}$	Liquid-Vapor
$\mathrm{H_2}$	Hydrogen
$\mathrm{N_2}$	Nitrogen
$\mathrm{O_2}$	Oxygen
class	classical system
quant	quantum system
sat	saturation
spn	spinodal
local	local
surf	surface energy
void	void
vol	volume (bulk) energy

Superscripts

*	Non-dimensional value (reduced by ε, σ, m)

References

[1] S. Kamiya, M. Nishimura and E. Harada, "Study on Introduction of CO2 Free Energy to Japan with Liquid Hydrogen", *Physics Procedia*, Vol. 67, pp.11-19, (2015).

[2] G. A. Zimmerli, M Asipauskas and N. T. V. Dresar, "Empirical correlations for the solubility of pressurant gases in cryogenic propellants", *Cryogenics*, Vol. 50, pp.556-560.

[3] J. Klier, C. Weichhard and P. Leiderer, "Wetting behaviour of solid and liquid hydrogen films", Physica B: Condensed Matter, Vol. 284, pp.391-392, (2000).

[4] K. Bellur, V. Konduru, M. Kulshreshtha, D. Tyrewala, E. Medici, J. S. Allen, C. K. Choi, D. S. Hussey, D. C. Jacobson, J. B. Leão, J. McQuillen, J. Hermanson and A. Tamilarasan, "Contact Angle Measurement of Liquid Hydrogen (LH2) in Stainless Steel and Aluminum Cells", *Journal of Heat Transfer*, Vol. 138(2), 020904, (2016).

[5] K. Kinugawa, "Path integral centroid molecular dynamics study of the dynamic structure factors of liquid para-hydrogen", *Chemical Physics Letters*, Vol. 292, pp.454-460, (1998).

[6] T. D. Hone and G. A. Voth, "A centroid molecular dynamics study of liquid para-hydrogen and ortho-deuterium", *The Journal of Chemical Physics*, Vol.121, pp.6412-6422, (2004).

[7] H. Nagashima, S. Tsuda, N. Tsuboi, A. K. Hayashi and T. Tokumasu, "A molecular dynamics study of nuclear quantum effect on diffusivity of hydrogen molecule", *The Journal of Chemical Physics*, Vol.147, 024501, (2017).

[8] H. Nagashima, S. Tsuda, N. Tsuboi, M. Koshi, K. Hayashi and T. Tokumasu, "An analysis of quantum effects on the thermodynamic properties of cryogenic hydrogen using the path integral method", *The Journal of Chemical Physics*, Vol. 140, 134506, (2014).

[9] J. Hord, R. B. Jacobs, C. C. Robinson and L. L. Sparks, "Nucleation Characteristics of Static Liquid Nitrogen and Liquid Hydrogen", Journal of Engineering for Power, Vol. 86, pp.485-494, (1964).

[10] M. Volmer and A. Weber, "Keimbildung in übersättigten Gebilden", Z. Phys. Chem., Vol. 119, pp.277-301, (1926).

[11] R. Becker and W. Döring, "Kinetische Behandlung der Keimbildung in übersättigten Dämpfern", *Ann. Phys*., Vol. 24, pp.719-752, (1935).

[12] P. G. Debenedetti, "*Metastable Liquids: Concepts and Principles*", Princeton University Press, (1996).

[13] M. Sekine, K. Yasuoka, T. Kinjo and M. Matsumoto, "Liquid-vapor nucleation simulation of Lennard-Jones fluid by molecular dynamics method", *Fluid Dynamics Research*, Vol. 40, pp.597-605, (2008).

[14] H. Watanabe, M. Suzuki and N. Ito, "Cumulative distribution functions associated with bubble-nucleation processes in cavitation", *Physical Review E*, Vol. 82, 051604, (2010).

[15] S. L. Meadley and F. A. Escobedo, "Thermodynamics and kinetics of bubble nucleation: Simulation methodology", *The Journal of Chemical Physics*, Vol. 137, 074109, (2012).

[16] J. L. F. Abascal, M. A. Gonzalez, J. L. Aragones and C. Valeriani, "Homogeneous bubble nucleation in water at negative pressure: A Voronoi polyhedra analysis", *The Journal of Chemical Physics*, Vol. 138, 084508, (2013).

[17] J. Diemand, R. Angélil, K. K. Tanaka and H. Tanaka, "Direct simulations of homogeneous bubble nucleation: Agreement with classical nucleation theory and no local hot spots", *Physical Review E*, Vol. 90, 052407, (2014).
[18] R. C. Tolman, "The Effect of Droplet Size on Surface Tension", *The Journal of Chemical Physics*, Vol. 17, pp.333-337, (1949).
[19] K. K. Tanaka, H. Tanaka, R. Angélil and J. Diemand, "Simple improvements to classical bubble nucleation models", *Physical Review E*, Vol. 92, 022401, (2015).
[20] D. W. Oxtoby and R. Evans, "Nonclassical nucleation theory for the gas-liquid transition", *The Journal of Chemical Physics*, Vol. 89, pp.7521-7530, (1988).
[21] X. C. Zeng and D. W. Oxtoby, "Gas-liquid nucleation in Lennard-Jones fluids", *The Journal of Chemical Physics*, Vol. 94, pp.4472-4478, (1991).
[22] T. Kinjo and M. Matsumoto, "Cavitation processes and negative pressure", *Fluid Phase Equilibria*, Vol. 144, pp.343-350, (1998).
[23] J. Navarro, F. Ancilotto, M. Barranco and M. Pi, "Toward a Density Functional Description of Liquid pH_2", *The Journal of Physical Chemistry A*, Vol. 115, pp.6910-6917, (2011).
[24] M. Pi, M. Barranco, J. Navarro and F. Ancilotto, "Nucleation and cavitation in parahydrogen", Chemical Physics, Vol. 399, pp.213-217, (2012).
[25] J. Cao and G. A. Voth, "The formulation of quantum statistical mechanics based on the Feynman path centroid density. II. Dynamical properties", The Journal of Chemical Physics, Vol.100, pp.5106-5117, (1994).
[26] A. Guirao, M. Centelles, M. Barranco, M. Pi, A. Polls and X. Viñas, "A density functional model for the surface properties of liquid ^{4}He", *Journal of Physics*: *Condensed Matter*, Vol. 4, pp.667-678, (1992).
[27] F. Dalfovo, A. Lastri, L. Pricaupenko, S. Stringari and J. Treiner, "Structural and dynamical properties of superfluid helium: A density-functional approach", *Physical Review* B, Vol. 52, pp.1193-1209, (1995).
[28] F. Ancilotto, F. Faccin and F. Toigo, "Wetting transitions of ^{4}He on alkali-metal surfaces from density-functional calculations", *Physical Review* B, Vol. 62, pp.17035-17042, (2000).
[29] J. W. Chan and J. E. Hilliard, "Free Energy of a Nonuniform System. III. Nucleation in a Two-Component Incompressible Fluid", *The Journal of Chemical Physics*, Vol. 31, pp. 688-699, (1959).
[30] C. S. Helrich, "*Modern Thermodynamics with statistical mechanics*", Springer, pp.190, (2009).
[31] K. P. Huber and G. Herzberg, "*Molecular spectra and molecular structure. IV. Constants of diatomic molecules*", Van Nostrand Reinhold Company, (1979).
[32] R. H. Swendsen, "*An Introduction to Statistical Mechanics and Thermodynamics*", Oxford University Press, pp. 245, 212, (2020).
[33] K. Huang, "*Statistical Mechanics*, 2nd Edition", John Wiley & Sons, (1987).
[34] Y. Kataoka, "Studies of liquid water by computer simulations. V. Equation of state of fluid water with Carravetta–Clementi potential", *The Journal of Chemical Physics*, Vol.87, pp.589-598, (1987).
[35] National Institute of Standards and Technology, NIST chemistry webbook, NIST (online), available from <http://webbook.nist.gov/chemistry>, (accessed on 2021/5/10).
[36] B. A. Younglove, "Thermophysical Properties of Fluids. I. Argon, Ethylene, Parahydrogen, Nitrogen, Nitrogen Trifluoride, and Oxygen", *Journal of Physical and Chemical Reference Data*, Vol. 11, Suppl. 1, pp.1-11 (1982).
[37] M. Barranco, M. Pi, A. Polls and X. Viñas, "The surface tension of liquid ^{3}He above 200 mK: A density functional approach", Journal of Low Temperature Physics, Vol. 80, pp.77-88, (1990).
[38] R. D. McCarty, J. Hord and H. M. Roder, "*Selected Properties of Hydrogen* (*Engineering Design Data*)", NBS Monograph 168, National Bureau of Standards, Boulder, CO, (1981).
[39] R. Schmidt and W. Wagner, "A new form of the equation of state for pure substances and its application to oxygen", *Fluid Phase Equilibria*, Vol. 19, pp. 175-200, (1985).
[40] E. W. Lemmon and S. G. Penoncello, "The Surface Tension of Air and Air Component Mixtures", *Advances in Cryogenic Engineering*, Vol. 39, pp. 1927-1934, (1994).
[41] S. Tsuda, T. Tokumasu and K. Kamijo and Y. Matsumoto, "Molecular Dynamics Study of Heterogeneous Bubble Nucleation in Liquid Oxygen Including Helium, Nitrogen, or Argon", *Proceedings of the 2002 ASME Joint U.S.-European Fluids Engineering Conference*, Vol. 257, pp. 455-460, (2002).
[42] R. Span, E. W. Lemmon, R. T. Jacobsen, W. Wagner and A. Yokozeki, "A Reference Equation of State for the Thermodynamic Properties of Nitrogen for Temperatures from 63.151 to 1000 K and Pressures to 2200 MPa", *Journal of Physical and Chemical Reference Data*, Vol. 29, pp.1361-1433, (2000).
[43] Ch. Tegeler, R. Span and W. Wagner, "A New Equation of State for Argon Covering the Fluid Region for Temperatures from the Melting Line to 700 K at Pressures up to 1000 MPa", *Journal of Physical and Chemical Reference Data*, Vol. 28, pp.779-850, (1999).
[44] M. Hermann and M. Saravi, "*Nonlinear Ordinary Differential Equations: Analytical Approximation and Numerical Methods*", Springer, (2016).
[45] V. K. Shen and P. G. Debenedetti, "Density-functional study of homogeneous bubble nucleation in the stretched Lennard-Jones fluid", *The Journal of Chemical Physics*, Vol. 114, pp.4149-4159, (2001).
[46] D. Chandler and P. G. Wolynes, "Exploiting the isomorphism between quantum theory and classical statistical mechanics of polyatomic fluids", The Journal of Chemical Physics, Vol. 74, pp.4078-4095, (1981).
[47] S. Fujikawa, T. Yano and M. Watanabe, "*Vapor-Liquid Interfaces, Bubbles and Droplets: Fundamentals and Applications*", Springer, (2011).
[48] H. Nagashima, "A Molecular Dynamics Study of the Quantum Effect on the Thermodynamic and Transport Properties of Liquid Hydrogen", Ph.D. Thesis, Tohoku University, (2014).
[49] Tuckerman, M., Berne, B. J. and Martyna, G. J., Reversible multiple time scale molecular dynamics, *The Journal of Chemical Physics*, Vol. 97, No.3 (1992), pp.1990–2001.
[50] G. J. Martyna, M. L. Klein and M. Tuckerman, "Nosé–Hoover chains: The canonical ensemble via continuous dynamics", *The Journal of Chemical Physics*, Vol. 97, pp.2635-2643, (1992).
[51] S. Maruyama and T. Kimura, "A Molecular Dynamics Simulation of Bubble Nucleation on Solid Surface", *Transactions of the*

Japan society of Mechanical Engineers Series B, Vol. 65, pp.3461-3467, (1999).
[52] S. Tsuda, T. Hirata, and H. Tanaka, A Molecular Dynamics Analysis of Homogeneous Bubble Nucleation with a Noncondensable Gas in Cryogenic Cavitation Inception, *Molecular Simulation*, Vol. 40, pp. 320-326, (2014).
[52] Y. W. Wu and C. Pan, "A molecular dynamics simulation of bubble nucleation in homogeneous liquid under heating with constant mean negative pressure", *Microscale Thermophysical Engineering*, Vol. 7, pp.137-151, (2003).